# Design, Fabrication, and Characterization of a Hybrid Integrated Photonic Module for a Synthetic Aperture Radar Receiver

Ahmad W. Mohammad , Chris G. Roeloffzen , *Member, IEEE*, Paul W. van Dijk , Lennart Wevers ,
Paolo Ghelfi , *Member, IEEE*, Manuel Reza , Tobias Otto , Hakimeh Mohammadhoseini , Rick Heuvink ,
Furkan Sahin , and Edwin Klein

*Abstract*—This article presents the design, fabrication, and characterization of the first photonic-assisted receiver module for a Scan-on-Receive synthetic aperture radar (SCORE-SAR) intended for Earth observation from space. The module is a hybrid photonic integrated circuit (PIC) that is designed to do precise and continuous beamforming-on-receive of wideband signals from a 12 antenna elements array, synthesizing up to three simultaneous beams. The PIC also implements frequency-agnostic photonic down-conversion so that the synthesized beams can be directly digitized. The PIC is realized by the hybrid integration of active chips on indium phosphide and a passive chip on silicon nitride. The design steps of the photonic module are discussed in this article, including: the functional designs, the optical mask designs, the filters designs, the printed circuit boards (PCB) design, and the control electronics that drive the PIC. Characterization and tuning of the different building blocks of the PIC is also presented, and frequency down-conversion functionality is experimentally demonstrated.

*Index Terms*—Beamforming, frequency conversion, photonic integrated circuits, synthetic aperture radar.

## I. INTRODUCTION

IN THE past few decades, Earth observation (EO) technology has provided crucial biological, physical, and chemical data, on a global scale, that was utilized in climate change research [1]. Also, EO plays a key role towards achieving sustainability goals through monitoring natural resources such as energy, freshwater, and agriculture [2].

Synthetic aperture radar (SAR) is a widely used spaceborne EO technique providing radar-enabled elevation images that, contrary to optical sensors, can be acquired independently of the weather conditions and the time of the day. Spaceborne SAR instruments work in various microwave frequency bands (P-band, L-band, S-band, C-band and X-band) depending on the application [3]. Lower microwave frequencies (C-band and lower) are used, for example, when larger penetration depths are needed which are useful for applications such as vegetation monitoring or soil moisture retrievals. Higher frequencies (X-band and in the future potentially Ka-band) allow for the use of larger bandwidths providing a better spatial resolution which is useful in urban planning applications, for instance.

Nowadays, advanced SAR imaging modes are implemented in spaceborne SAR sensors which benefit from the implementation of the beam steering capabilities in the SAR instrument. Beam steering is typically achieved by RF analog, digital or hybrid approaches [4], [5]. Cost, size, and power consumption are some of the challenges associated with digital beam steering, which limits its use to large spacecrafts. With the latest advances of microwave photonics [6], [7], specifically the photonic integrated circuit (PIC) technology [8], radar beam steering implementations in the photonics domain offer an attractive alternative due to its compactness, broadband nature, immunity to EMI, and low loss [9], which can make SAR available in small missions.

Future spaceborne SAR instruments require the instantaneous imaging of a wide swath at a high resolution which can be realized by advanced SAR imaging modes such as the scan-on-receive (SCORE) [10]. Fig. 1 illustrates the SCORE concept, where a wide swath is illuminated in the transmit mode, and multiple simultaneous receive beams are steered in the receive mode across the swath to receive the radar echoes stemming from different transmit events [11].

This article discusses the design and implementation of the first photonics-assisted SCORE-SAR receiver module, which is done within SPACEBEAM project (Space SAR system with reconfigurable integrated photonic beamforming) [12]. The project aims at achieving a swath 5 times wider than the current
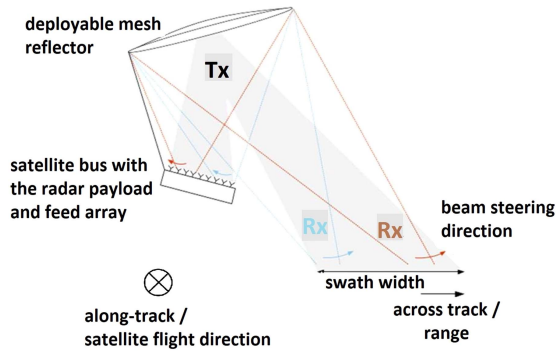
Fig. 1.   Illustration of the SCORE imaging mode [11].

spaceborne SAR systems, while, at the same time, guaranteeing 1.5 m spatial resolution on both along- and across-track directions [13]. SPACEBEAM promises to consume low power, thanks to the hybrid photonic integration technology and the use of the Lead Zirconate Titanate (PZT) actuators [14], where the total power consumption per receiver module is estimated at 3.5 W [15]. Further, SPACEBEAM provides reconfigurable $12 \times 3$ beamforming and signal down-conversion functionalities, by exploiting the reconfigurable Blass matrix [15], [16], [17], [18], [19], [20]. The initial target frequency is 9.65 GHz in the X-band with a minimum bandwidth of 450 MHz, but there are no limitations to extend this work to higher frequencies, such as the Ka-band.

The rest of the article is organized as follows: Section II discusses the design steps starting from the preliminary architecture up-to the masks designs of the hybrid assembly and the printed circuit board (PCB) that surrounds it as well as the control electronics that drives the assembly, while Section III is dedicated to fabrication, showing the produced chips and the building of the hybrid assembly and mounting it on the control electronics box. Then, the testing and characterization results are presented and analyzed in Section IV, showing the tuning of the different building blocks and demonstrating the frequency down-conversion functionality. Finally, Section V provides a summary of the article and an outlook on the future work.

## II. DESIGN

The goal is to design a $12 \times 3$ beamformer for a SCORE-SAR receiver in the X-band at 9.65 GHz with minimum bandwidth of 450 MHz and a down-conversion capability to a low intermediate frequency (IF = 1.35 GHz). To achieve this goal, a preliminary architecture of the PIC is proposed (Fig. 2), where a continuous wave optical signal is modulated by an electronic local oscillator (LO) to generate three locked optical signals (a carrier and two side tones), which are amplified by a semiconductor optical amplifier (SOA), separated, and filtered (to reduce the amplified spontaneous emission (ASE) noise from the SOA). The carrier is split into 12 branches to modulate 12 RF input signals from 12 input antennas. Then, a $12 \times 3$ Blass switching matrix is used to perform delay, phase and amplitude control to the modulated signals and to combine them to form the receiving

beams [19], [20]. Finally, the outputs of the Blass matrix are filtered, to select one of the two sidebands, and heterodyned in the photodiodes, with one of the side tones of the first modulator to down-convert the received RF signal into an IF, which is equal to the difference between RF and LO, and is ready for amplification/filtering and digitization at the analog to digital converter (ADC).

The proposed design combines active components on indium phosphide (InP) and passive component on silicon nitride ($Si_3N_4$). More specifically, the proposed PIC is a hybrid integration of the following chips:

- *InP gain chip:* serves as a gain section of the laser.
- *InP modulators chips:* arrays of modulators for electrical to optical (E-O) conversion of the LO and the RF signals. These modulators have 40 GHz bandwidth, and they are monolithically integrated with SOAs to boost the optical signals powers.
- *Si₃N₄ chip (TriPleX):* provides low-loss waveguides [21], for the laser cavity, signal filtering, signal splitting and combining, and optical beamforming.
- *InP photodiodes (PDs) chip:* an array of photodiodes with a bandwidth of up to 40 GHz to realize optical to electrical (O-E) conversion.

### A. Analytical Analysis of the RF Gain

Several detailed design flavors could be derived from the preliminary architecture of Fig. 2. A number of such candidate schemes have been analyzed mathematically and simulated in VPIphotonics to compare their RF gain performances. Differences between these design flavors are related to how laser power splitting is realized between the LO and RF modulators, as well as the number of SOAs and their locations. Out of 10 simulated schemes, two schemes were favored because they offer distinct advantages: the first scheme provides the highest RF gain, while the second scheme requires only half the LO frequency, which is important when extending this work to higher frequencies.

In the first scheme, which is shown in Fig. 3, the laser power is split, by a tunable coupler, between the LO modulator and the RF modulators, which are monolithically integrated with SOAs. The tunable coupler should be set such that the power at the LO modulator input is just below the saturation limit, while the remaining laser power is directed to the RF modulators' path. A variable optical attenuator (VOA) is placed in the path towards the RF modulators in order to avoid the possibility of saturating their input SOAs. The modulators are push-pull Mach–Zehnder modulators (MZM) and they have two outputs, so, when biased at the null point, they direct the odd order sidebands to the desired output (with SOA), and the carrier and the even modes to the other port [22], so that the SOA would not be saturated by the carrier. After modulation and amplification, the RF modulated optical signals are combined in the Blass matrix, and then, heterodyned with the optical LOs in the PDs.

More specifically, assuming that an 18 dBm optical signal is generated by the laser and split equally, by a TriPleX-based tunable coupler, between the paths of the LO modulator and the RF modulators. On the LO path, assuming that the TriPleX
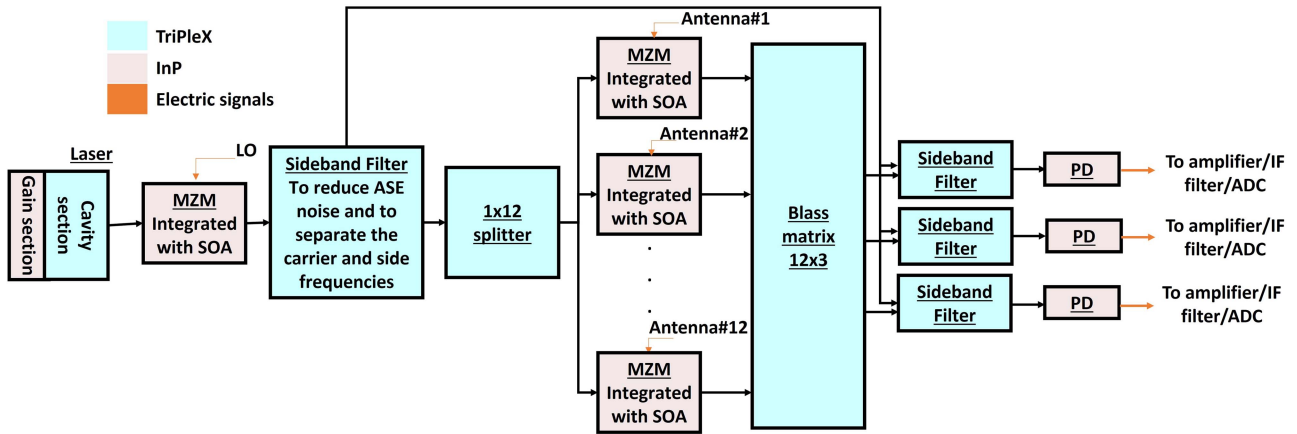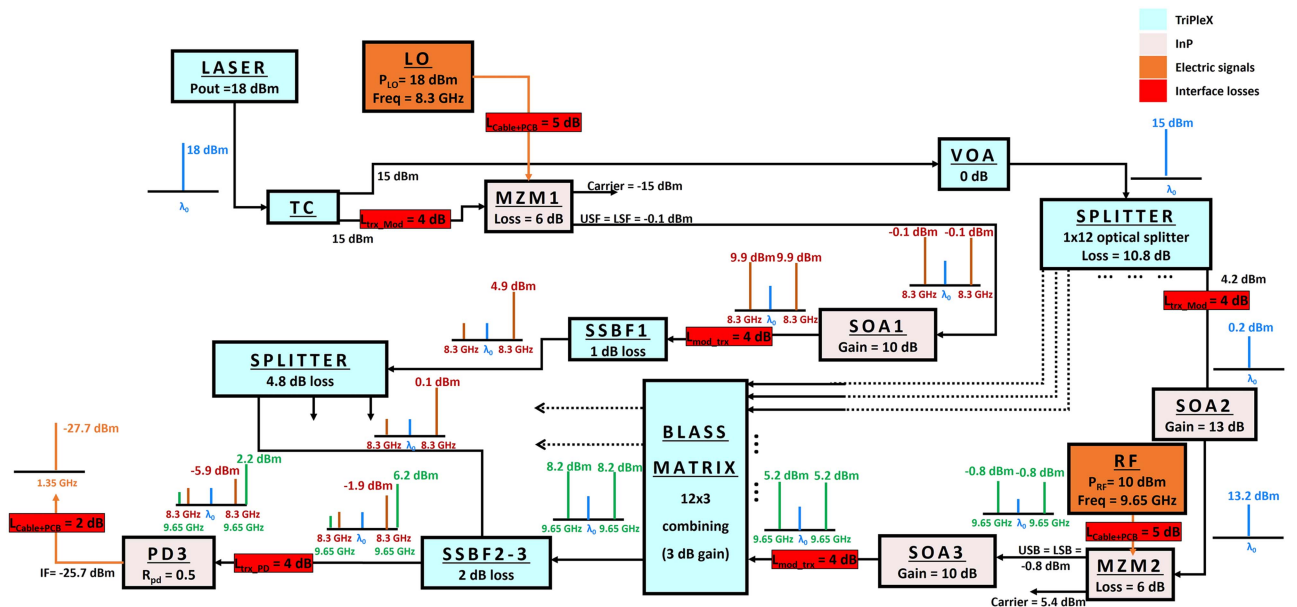
Fig. 2. Preliminary architecture of the PIC.



Fig. 3. First candidate design of the hybrid assembly.

to MZM chip interface loss is 4 dB, and that the propagation loss in the MZM is 6 dB, then, the LO MZM will generate two side frequencies of $-0.1$ dBm each, when it is driven by an electrical LO of 18 dBm (13 dBm considering PCB and cables losses) at 8.3 GHz. A SOA at the LO MZM output with a gain of 10 dB amplifies the side frequencies to 9.9 dBm each, after which, a filter is used to select only one of the side frequencies, which is then split into three, corresponding to the three PDs. On the RF path, when the VOA is set to 0 dB attenuation, the 15 dBm carrier will get split by a $1 \times 12$ splitter, thus, losing 10.8 dB, and gets coupled to the RF modulator chip, where the coupling losses are 4 dB. So, the carriers will reach the MZM chip with a power of 0.2 dBm, where it gets amplified by the integrated input SOA to 13.2 dBm. An RF signal of 9.65 GHz and 10 dBm (5 dBm considering losses in the cables and the PCB) is assumed at each modulator input, thus, two sidebands of $-0.8$ dBm each are generated at one of the output ports which also has an integrated SOA, so, they are amplified to 9.2 dBm

each. Due to the MZM chip to TriPleX interface losses (4 dB), the sidebands reach the next stage – the Blass matrix – with a power of 5.2 dBm each. The gain of the Blass matrix has been simulated for the $12 \times 3$ combining scenario and is presented in a previous publication [15]. In that analysis, the gain was calculated against the total power from 5 inputs, and it fluctuated around $-4$ dB depending on the angle of the beam. On the other hand, the power considered in this article is from a single RF input, therefore, the gain here is 5 times higher (7 dB higher) than in [15], that is, 3 dB. So, each one of the three outputs of the matrix will contain double sideband signals, 8.2 dBm each, which are combined, by the three filters, with the three signals from the LO path, and heterodyned in the three PDs. Assuming a TriPleX to PD coupling losses of 4 dB, the optical RF and LO will reach the PD with powers of 2.2 dBm and $-5.9$ dBm, respectively. For a uni-traveling carrier photodiode (UTCPD) with a typical responsivity of 0.5 A/W, this results in a $-25.7$ dBm IF at 1.35 GHz. Finally, assuming 2 dB loss in
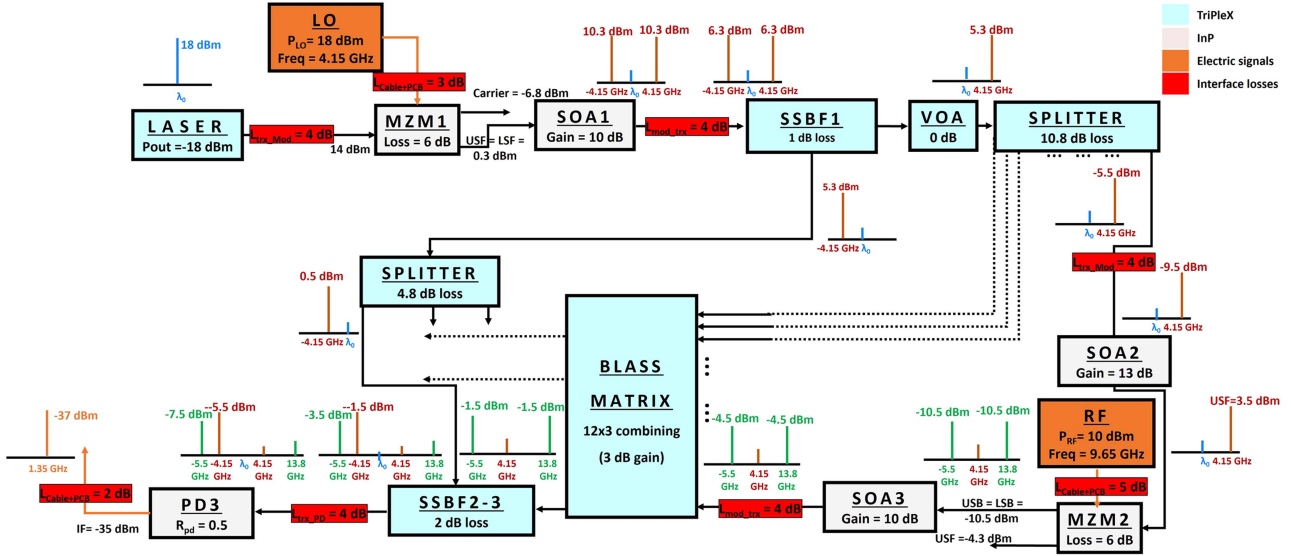
Fig. 4.  Second candidate design of the hybrid assembly.

the IF path due to propagation losses in the PCB and the cables, then, an IF of −27.7 dBm should be measured on the electrical spectrum analyzer (ESA).

In the second scheme, shown in Fig. 4, there is no laser splitting. Instead, the laser power is directed to the LO MZM, which is modulated with an electrical LO of 4.15 GHz and 18 dBm (15 dBm considering the cables and PCB losses at 4.15 GHz). Similar to the first scheme, the LO MZM is biased at the null point to direct the carrier to one output port, and the lower/upper side frequency (LSF/USF) to the other output port, where they get amplified by a 10 dB-gain SOA to 10.3 dBm each. A filter is used to separate the LSF and the USF such that the USF is directed via the 1 × 3 splitter to the three PDs, while the LSF is directed to the RF modulators. Contrary to the first scheme where the carrier is used to drive the RF modulators, the second scheme uses the LSF instead. The advantage of this configuration is that it provides a similar function as the first scheme while requiring only half of the LO frequency. Considering the loss due to the 1 × 12 splitting (10.8 dB) and the TriPleX to MZM coupling losses (4 dB), the LSF reaches the input SOA of the RF modulator with a power of −9.5 dBm. The LSF is then amplified with the 13 dB-gain SOA, modulated with the RF MZM to generate sidebands with −10.5 dBm each. The sidebands are then amplified with a 10 dB-gain SOA, combined in the Blass matrix, filtered with the sideband optical filter, and heterodyned in the PDs with the USFs coming from the LO path. Given that the TriPleX to the PD chip coupling loss is about 4 dB, the powers of the beating signals at the PDs will be −7.5 dBm and −5.5 dBm for the USF and the upper sideband, respectively, thus, generating a −35 dBm IF signal at 1.35 GHz. Again, assuming 2 dB of propagation losses in the PCB and the cables, then, −37 dBm IF should be measured with the ESA. The RF gain in this scheme is lower than that in the first scheme, but it requires half the LO frequency, which is an advantage, especially when extending this work to higher frequencies.

## B. PIC Layout

The next step is to translate the previous two schemes into PIC layouts. The goal, here, is to create one generic layout that can realize both schemes. This is made possible by adding a tunable coupler at the output of the laser. By changing the coupling ratio of the tunable coupler, it is possible to switch between the two schemes. This is illustrated in Fig. 5(a) and (b), which correspond to the first scheme and the second scheme, respectively, where the TriPleX chip is placed in the center and all the active InP chips are attached around it. As will be shown later, the assembly will also have two fiber arrays on the left and the right sides (FAL & FAR) to help characterizing and tuning it. For example, the optical port FAL8 (in Fig. 5) is for monitoring the output of TC2.

## C. Filters Design

The challenge, then, is to design the first filter (SSBF1) and the second filters (SSBF2) in a way that is suitable for both schemes, since, in the first scheme, SSBF1 is required to select only the USF at 8.3 GHz, while, in the second scheme, it should pass the USF and the LSF at 4.15 GHz at the first and the second output ports, respectively. As for the second filters (SSBF2), they should combine the optical LO at 8.3 GHz with the RF sideband at 9.65 GHz in the first scheme, and the optical LO at 4.15 GHz with the RF sideband at 5.5 GHz in the second scheme.

Filters modeling and simulations have been implemented in LabVIEW to check whether both configurations could be achieved by one filter design and to determine the physical parameters of such a filter. The simulations concluded that, indeed, it is possible to satisfy the conditions of the two schemes with one filter of the fifth order: a Mach Zehnder interferometer (MZI) and two rings, as sketched in Fig. 6.

For SSBF1, simulations concluded that each ring should be 10.5 mm long. However, it is not possible to achieve such a small length in the PZT-based TriPleX design since the minimum
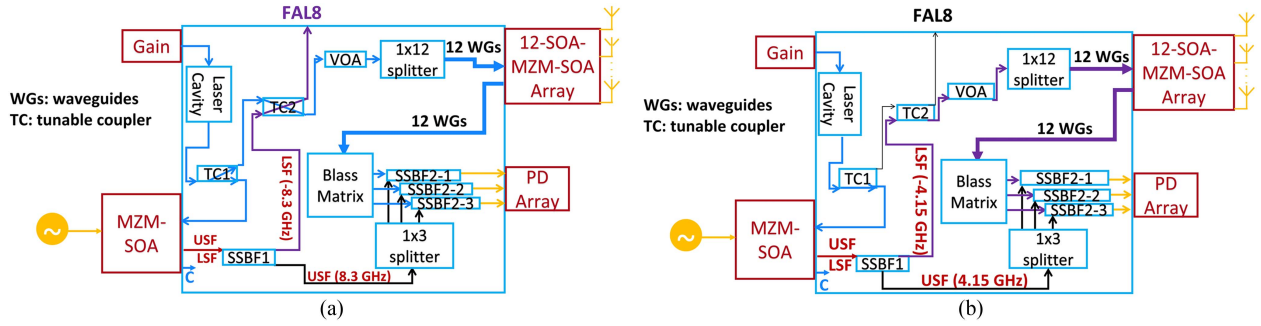
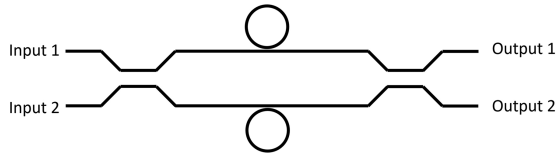Fig. 5.    PIC layout. First scheme (a) and second scheme (b).



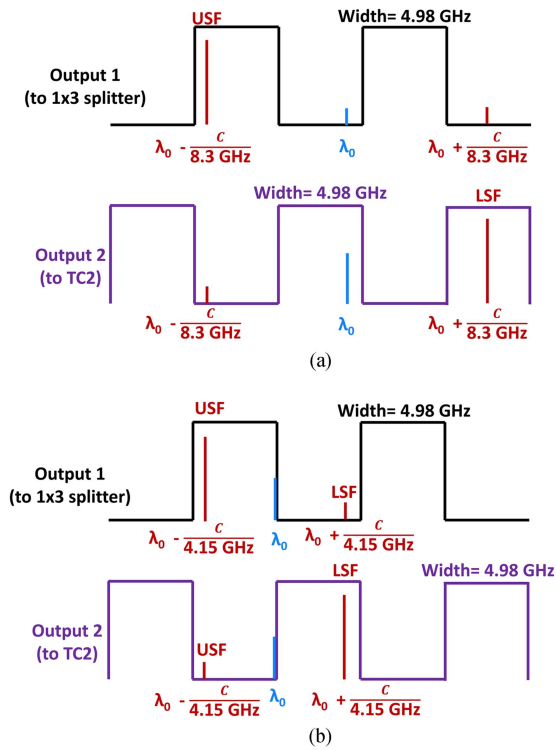Fig. 6.    5th order filter implementation.



Fig. 7.    Illustration of suitability of SSBF1 for the first scheme (a) and the second scheme (b).

length of the ring is determined by the length of the PZT itself, which is approximately 15 mm, and that defines the minimum length for the ring to at least 25 mm [14]. Keeping this constraint in mind while simulating the filter in LabVIEW, it was possible to design the filter with rings that are 34 mm long. This resulted in a filter with a passband width of 4.98 GHz. The filter response is sketched in Fig. 7(a) and (b) to illustrate its suitability for the first and the second schemes, respectively. As shown in Fig. 7(a),

the 8.3 GHz USF passes through output 1 of the filter to the $1 \times 3$ splitter while the carrier and the LSF are suppressed in this port, but they pass through the other port (output 2) towards the tunable coupler (TC2), which directs them to the outside of the system when TC2 is set to the cross state. In the second scheme, illustrated in Fig. 7(b), both the USF and LSF need to pass to the rest of the system from a different output port. This is realized by positioning the carrier in the transition band of the filter. This allows the 4.15 GHz USF to pass through the first port, and the LSF to pass through the second port, while the carrier is suppressed by properly biasing the MZM at the null point. In this case, the tunable coupler (TC2) needs to be in the bar state to direct the LSF to the VOA and then to the rest of the system.

A similar design procedure was followed to design the second filter (SSBF2). This filter should be very selective because it will combine optical signals that are 1.35 GHz apart. Since this filter is very selective, the length of rings had to be large (100 mm), which resulted in a passband width of 1.69 GHz. Here too, the filter needs to be suitable for both schemes. In the first scheme, the filter combines the 9.65 GHz signal from the Blass matrix output with the 8.3 GHz signal from the $1 \times 3$ splitter output, as illustrated in Fig. 8(a). In the case of the second scheme, the filter combines the USF at 4.15 GHz from the $1 \times 3$ splitter output with the sideband RF signal at 5.5 GHz from the Blass matrix, which is the result of modulating the LSF at 4.15 GHz by a 9.65 GHz RF, as illustrated in Fig. 8(b).

### D.  Chips Design

The chip layout described in the previous section has been translated into photonic mask design. The dimensions of the TriPleX chip are 22 mm X 22.7 mm. The hybrid assembly design is depicted in Fig. 9, showing TriPleX chip in the center, the two fiber arrays, and the InP chips that are attached to TriPleX. The figure also highlights the number of RF connections, which are of ground-signal-ground (GSG) type, and the DC connections required by every chip, which is needed to design the PCB. Based on this design, a 3D drawing of the hybrid assembly has been generated; It is shown in Fig. 10. Here, it is worth mentioning that, for optical LO generation, a 4-MZM-SOA array chip is used, although only one MZM-SOA is needed. Similarly, a 4-PD array chip is attached instead of a 3-PD array. This is due to the
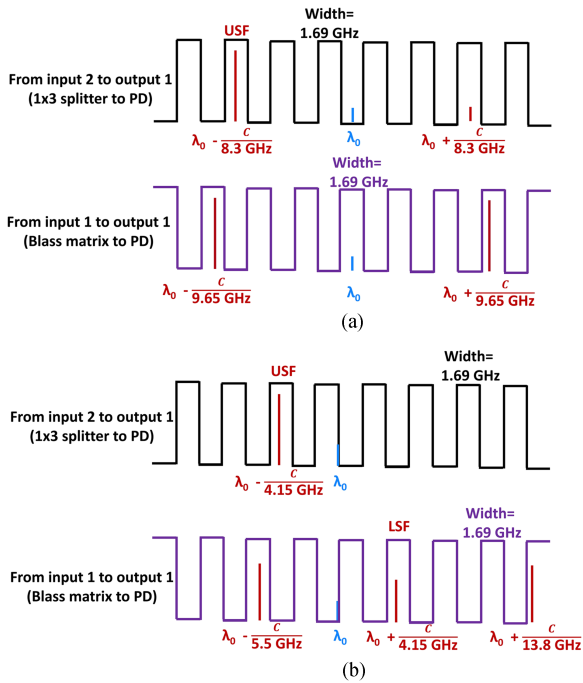
Fig. 8. Illustration of suitability of SSBF2 for the first scheme (a) and the second scheme (b).
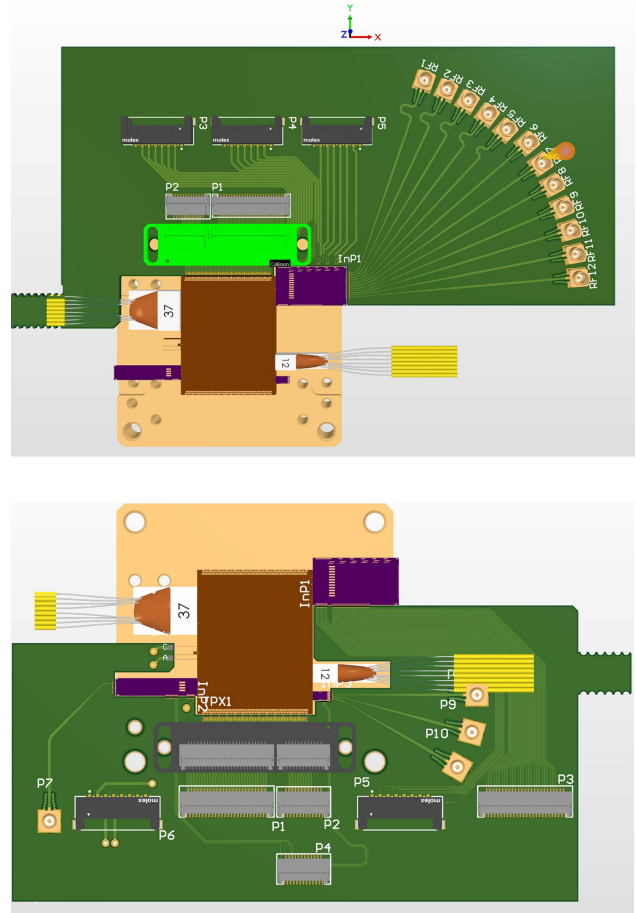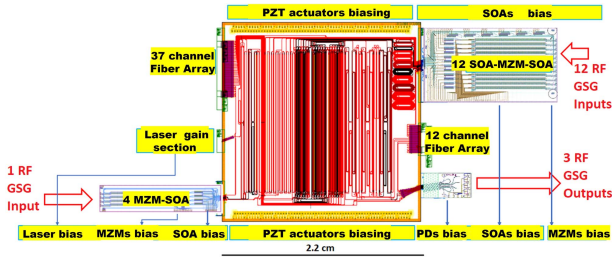


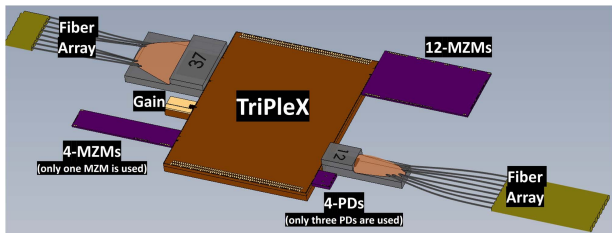Fig. 9. Mask design of the hybrid assembly.



Fig. 10. 3D model of the hybrid assembly.

unavailability of arrays of the same size as in the functional design.

LioniX International (LXI) designed a PCB around the hybrid PIC with DC traces and connectors to bias the different sections on the PIC, as well as RF transmission lines and connectors to apply the RF signals and the LO to the modulators and to readout the IF signals from the PDs. To facilitate the assembly process later, the PCB design was made with two parts (north and south), and they are shown in Fig. 11.



Fig. 11. Designed PCB to access the hybrid assembly.

## III. FABRICATION

Before building the hybrid assembly, the individual chips were tested to make sure they have no defects. First, each InP chip has been visually inspected, to make sure there are no defects in the optical waveguides, then, DC-tested against electrical defects. In a functioning chip, a 50 Ω termination resistance should be measured and the PN junctions should exhibit a diode response (0.7 V in one polarity and an open loop in the opposite polarity). Also, TriPleX has been tested for waveguides defects both visually and by injecting light to the chip and looking for scattering points from defective waveguides. Then, LXI used the chips that passed the tests to build the hybrid assemblies by attaching the InP chips and the fiber arrays to TriPleX chip, as shown in the photo of Fig. 12. A glass plate has been glued on the top of TriPleX chip to protect the PZT actuators from dust and moisture, since these factors can reduce the lifetime of the actuators.

After that, LXI mounted the hybrid assembly and the PCB onto a copper block and wire-bonded them. The result is shown in Fig. 13. For temperature control, the copper block is designed with a hole to insert a thermistor, and the copper block is placed on top of a Peltier element, which, in turn, is placed on top of a cooling block.
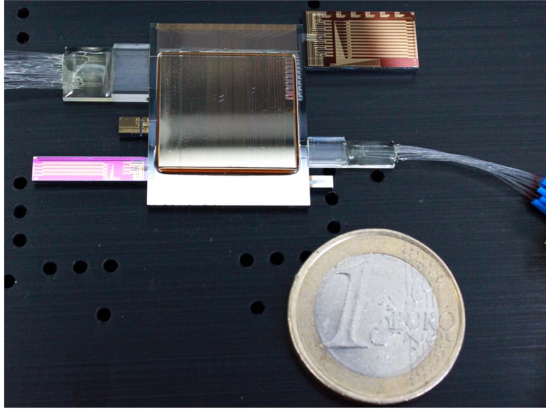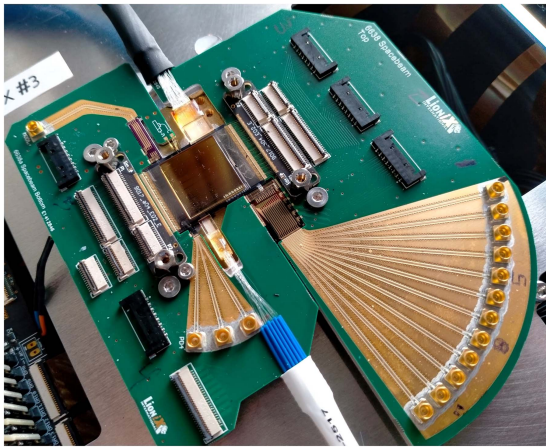
Fig. 12.　Photo of the hybrid assembly.



Fig. 13.　Photo of the hybrid assembly after wire-bonding to the PCB.
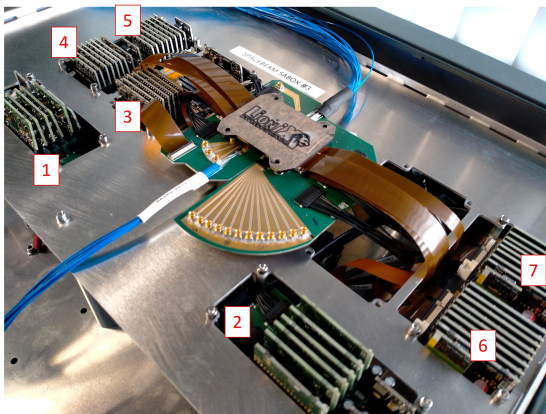


Fig. 14.　Photo of the hybrid assembly and the surrounding control electronics: (1 and 2) are current sources for the laser and the SOAs. (3) is for biasing the modulators and photodetectors. (4, 5, 6, and 7) are for biasing the PZT actuators.

For the driving of the PIC, LXI developed the driving electronics (called SaBox), which can be used to drive all the components in InP and TriPleX chips. The control electronics was designed in a modular fashion, as shown in Fig. 14, where each group of electronic cards is designated to driving certain sections in the hybrid assembly. For example, in Fig. 14, module 1 and module
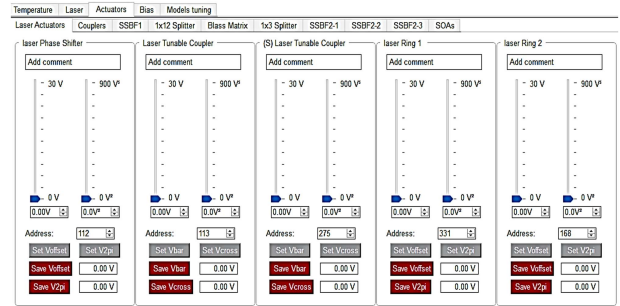


Fig. 15.　Example screenshot from the control electronics software.

2 are designed to provide relatively high currents (300 mA) per laser and per SOA and are connected to the PCB via 8-pin black cables, while module 3 is designed to bias the modulators and the PDs with low voltage and low current (up to 10 V, up to 10 mA) and are connected to the PCB via the brown flat cables, shown in the same figure. Finally, the rest of the modules are designed to drive the PZT actuators on TriPleX with high voltage and low current (up to 40 V, 1 uA) and they are also connected to the PCB via the brown flat cables.

The driving electronics box must be connected to a computer via a USB cable. Each of the electronic boards has a USB-to-serial chip onboard, to translate the messages to and from the microprocessor. The commands can be sent as ASCII serial commands from typical serial port terminal software. LXI also developed a software tool with graphical user interface (GUI) with several tabs to control the chips. An example is shown in Fig. 15. The first tab contains a slider and a button for the temperature control, and a slider to control the speed of the fan attached to the heatsink beneath the assembly. Other tabs contain sliders to control different sections on the chip, such as modulators biases, PZT actuators, and SOAs. All of the settings can be saved, and saved settings can be recalled.

## IV. Characterization Results

For the experimental part, it was decided to tune the system according to the second scheme since the tunable coupler (TC2) got broken during characterization, and its default state is bar, which is compatible with the second scheme, as shown earlier in Fig. 5(b).

### A. Laser Characterization

The laser consists of a single gain section in InP and a cavity in TriPleX comprising a phase section, two rings, and a tunable coupler [23]. The laser was tunable between 1527 nm and 1560 nm, by tuning the current applied to the gain section, the voltage applied to the different sections of the TriPleX cavity, and the temperature of the assembly.

A peak power of $-11.8$ dBm has been measured on the optical spectrum analyzer (OSA) at 1537.2 nm, with 60 dB side mode suppression ratio (SMSR), as shown in the spectrum in Fig. 16, which is measured at the monitoring port of TC2 (FAL8). For the rest of the measurements, the temperature of the assembly was set to 30 °C, and the laser was tuned to 1537.2 nm because
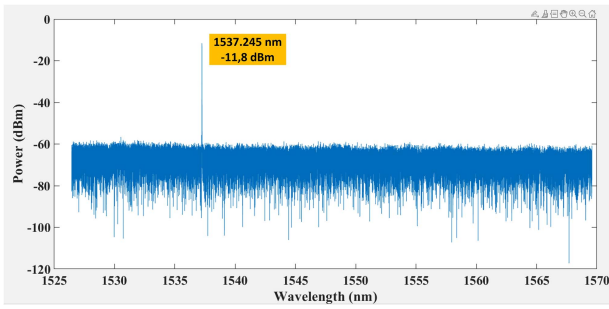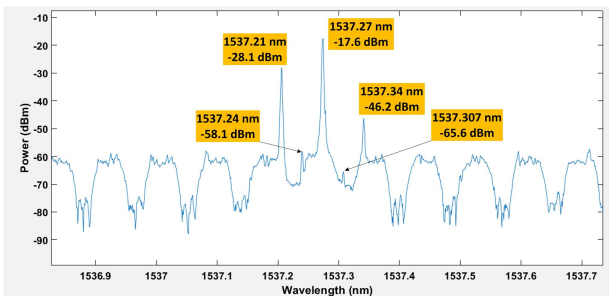
Fig. 16.    Measured laser spectrum.



Fig. 17.    LO filter tuning.



Fig. 18.    SSBF2-3 tuning using the VNA.



Fig. 19.    VNA spectrum showing the system gain versus intermediate frequency (IF).

the SOAs in the following stages provided more gain at this wavelength than around 1550 nm, for example.

### B. LO Filter (SSBF1) Tuning

The next step is tuning the LO filter (SSBF1). This is done by turning on the SOA at the output of the LO modulator, and using its ASE noise as a broadband optical source, while applying a 4.15 GHz LO from a signal generator, and monitoring the optical signal at the output of the VOA. Filter shaping is done by tuning its tunable couplers, rings, and phase shifters. The goal is to tune the filter such that the LSF is maximized, while the USF is minimized at this port. Due to the complimentary nature of the filter response, the USF will be maximized on the other output port of the filter. Fig. 17 shows the optical spectrum after tuning, where the power of LSF is −17.6 dBm and the power of the USF is −28.1 dBm. The difference between them (10.5 dB) is less than the extinction ratio of the filter (∼15 dB). This can be explained by the wide transition band of the filter, which caused the USF to fall in the transition band, and therefore, only getting partially suppressed. This could be improved by more fine tuning of the filter (20 dB suppression is possible), and by making a higher quality filter with sharp transition bands by reducing the propagation losses in the optical waveguides. Further, Fig. 17 shows a suppressed carrier of −58.1 dBm and a suppressed 2nd order harmonic of −65.6 dBm. The 2nd order harmonic is suppressed despite being in the passband of the filter because the MZM is biased such that the even modes are directed to its other output port. Finally, Fig. 17 shows a weak 3rd order harmonic of −46.2 dBm on the LSF side, so, it will not cause interference in the band of interest.
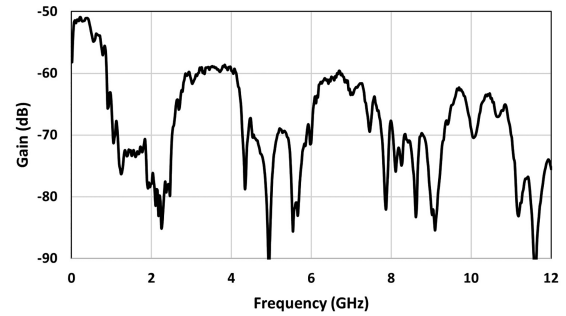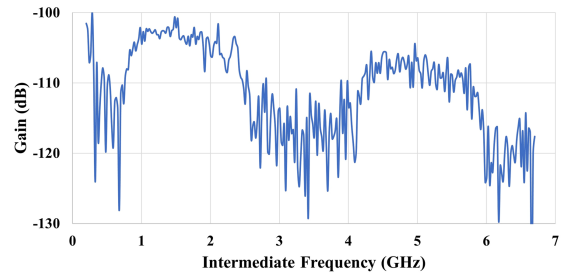
After that, the $1 \times 12$ splitter and the Blass matrix had to be tuned. Since the experimental part of this article focuses on demonstrating signal down conversion functionality rather than beamforming, the $1 \times 12$ splitter was tuned such that the power at its input is directed to one modulator (modulator_6) rather than splitting it equally between the 12 modulators. The input and output SOAs of this modulator were turned on (79.9 mA and 95.4 mA, respectively). Then, the tunable couplers in the Blass matrix were tuned such that the signal from the output of modulator_6 is directed to the SSBF2-3 in the following stage.

### C. SSBF2-3 Tuning

As shown in Fig. 5, the third output of the Blass matrix goes to the SSBF2-3, and then, to a PD in the next stage, which, in turn, can be connected to an ESA or a vector network analyzer (VNA). For the tuning of the SSBF2-3, a 10 dBm sweeping RF signal was applied to modulator_6 from the sending port of a VNA, while the receiving port of the VNA was connected to the PD. Here, no signal was applied to the LO modulator. Tuning SSBF2-3 is achieved by tuning its tunable couplers, rings, and phase shifters. The VNA spectrum of the filter after tuning is shown in Fig. 18. The  filter has a passband of about 1.7 GHz, as expected by the design (Fig. 8). The VNA spectrum shows a drop in the measured power as a function of frequency, in addition to a signal distortion at about 10 GHz. These effects are due to the frequency responses of the cables and the PCBs.

### D. Demonstration of Frequency Down-Conversion

To demonstrate the down-conversion functionality, the laser, the LO and the RF modulation were all turned on. A 54.3 mA current was applied to the gain section of the laser. The electrical
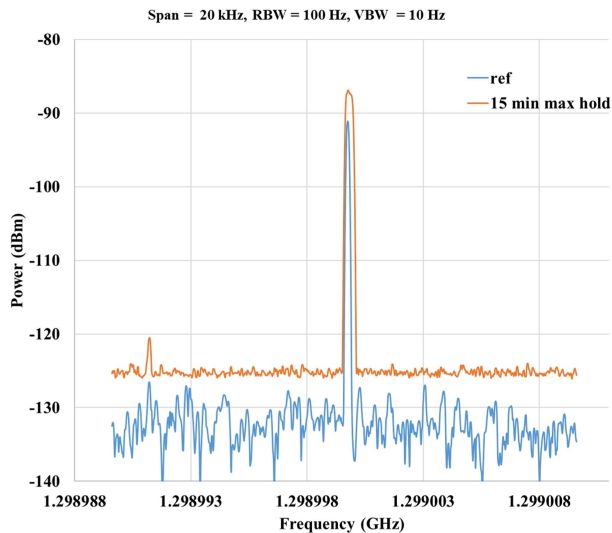
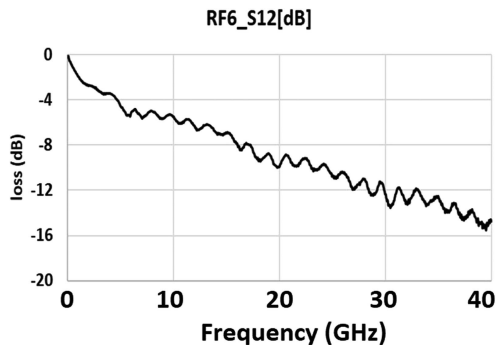Fig. 20.    Stability measurement of the down-converted signal.



Fig. 21.    RF losses in the PCB in modulator_6 path.

LO was provided by a signal generator that was set to 4.15 GHz and 18.5 dBm, and the SOA after the LO modulator was biased with 94.6 mA, while a sweeping RF signal from 8.5 GHz to 15 GHz was applied from the VNA to modulator_6, and the down-converted signal was read by the VNA at the PD output. The settings for the input and output SOAs of modulator_6 were 79.9 mA and 95.4 mA, respectively. The down-converted spectrum is shown in Fig. 19. The down-conversion gain is about −104 dB, which includes the losses in the RF cables and the PCB.

To check the stability of the system, a 10 dBm RF signal at 9.59 GHz was applied to modulator_6, and the down-converted signal was measured on an ESA at 1.29 GHz. Then, the max hold setting was turned on for 15 minutes. Fig. 20 plots both the reference measurement and the max-hold measurement. The ESA has the following settings: span = 20 kHz, RBW = 100 Hz, VBW = 10 Hz. It can be concluded from the figure that the system was stable during the measurement.

### E.  Analysis of Results

There is a big deviation between the calculated RF gain in Fig. 4 (−47 dB) and the measured RF gain of Fig. 19 (−104 dB).

This is mainly due to the low measured laser power (−11.8 dBm) compared to the 18 dBm used in the calculations, the extra optical losses in the modulators, and the extra losses in the PCBs.

The 18 dBm output power from the laser was based on typical experimental data from LioniX International lasers [23]. However, these lasers were all designed with heater-based actuators while, in this work, the laser actuators are PZT-based. Although this is considered as a major breakthrough since it is the first demonstration of a PZT-based laser, the measured power was much lower than expected. There are two main contributing factors to this lower power. First, the propagation losses in this TriPleX fabrication run were higher than the typical (0.2 dB/cm instead of 0.06 dB/cm), and second, the length of the PZT actuator is much longer than its heater counterpart (1.5 cm instead of 1 mm), which resulted in extra losses in the laser cavity.

Regarding the optical losses in the modulators, a value of 6 dB was assumed in the calculations of Figs. 3 and 4, which was the target design value. However, the measured loss was about 9 dB.

Further, the measured losses in the PCB were more than expected. Fig. 21 shows an example of the S12 measurement in the RF trace of modulator_6. It gives 6 dB loss at 9.6 GHz. As for the LO path, 2.8 dB loss is measured at 4.15 GHz, while 1.8 dB loss is measured in the IF path of the PCB at 1.35 GHz. Also, the losses in the cables need to be taken into account. These are 5 dB at 9.6 GHz for the RF path, 3 dB at 4.15 GHz for the LO path, and 1 dB at 1.35 GHz in the IF path.

Based on the previous discussion, a new system model can be constructed. Fig. 22 shows a similar analysis to that done in Fig. 4 but with experimental values. In the experimental demonstration of 1 RF to 1 PD down-conversion, the couplers of the $1 \times 3$ splitter and the $1 \times 12$ splitter were tuned to maximize the power at one output port only, namely, at PD3 input and modulator_6 input, respectively. Here, 1 dB loss and 2 dB loss are assumed in the $1 \times 3$ splitter and the $1 \times 12$ splitter, respectively, due to propagation loss and imperfect tuning. In that case, the USF should reach the PD with a power of −28.6 dBm (assuming 2 dB of loss in the SSBF2-3 and 4 dB of coupling losses between the TriPleX and the PD chips). As for the LSF, it should reach the RF modulator chip with a power of −27.6 dBm, where it gets amplified to −17.6 dBm (assuming 10 dB gain input SOA) and new sidebands are created with a power of − 39.9 dBm each, which in turn, get amplified by the output SOA, to −26.9 dBm each. Again, assuming 4 dB TriPleX to modulator chip coupling losses, 3 dB loss due to propagation losses and the imperfect tuning of the Blass matrix, 2 dB loss in SSBF2-3, and 4 dB TriPleX to PD coupling losses, then, the RF sideband signal should reach the PD with a power of −39.9 dBm. Typically, the UTC-PD has a responsivity of 0.50 A/W, so, heterodyning −28.6 dBm LO with −39.9 dBm RF should result in an IF of −90.5 dBm.

Considering the losses in the PCB and the cables in the IF path, −93.5 dBm IF should be measured at the ESA. Finally, taking into account the losses in the cables and the PCB in RF path (11 dB), an RF gain of −104.5 dB is obtained, which is close to the measured gain in Fig. 19.
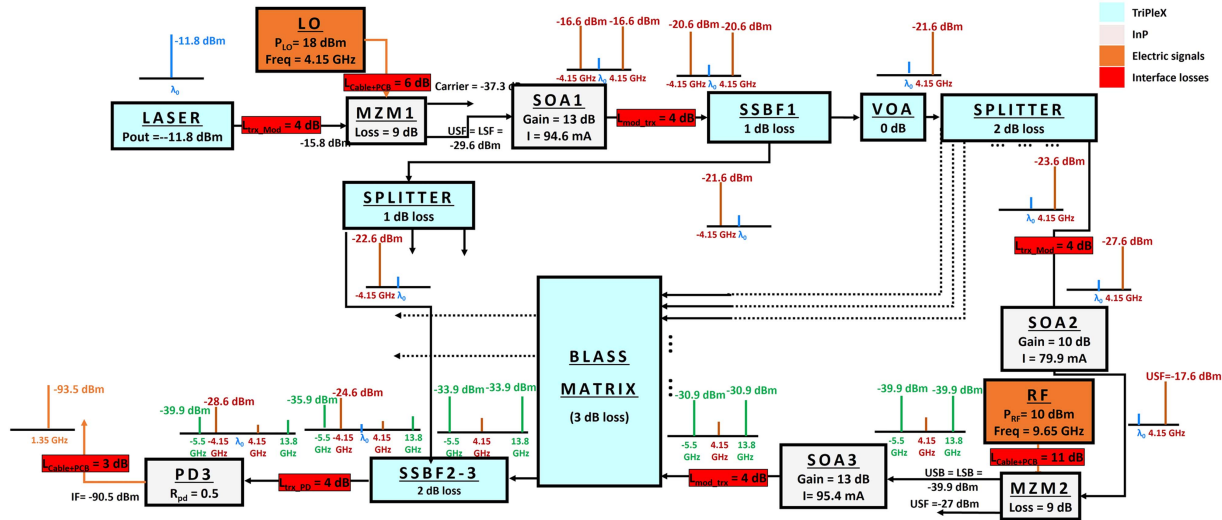
Fig. 22.    Signal propagation model based on experimental data.

The input optical powers to the SOAs in the experimental based model are much lower than those in initial models of Figs. 3 and 4, so, it is reasonable to assume higher SOA gain in the experimental based model. However, in the experiments, the SOAs were biased with lower currents ($\sim$80 mA, $\sim$95 mA) than the nominal values (300 mA), so, eventually, the same values of gain were adopted for both models. The decision to use lower bias currents was because working with high currents produced new laser lines due to reflections.

## V. Conclusion

This article presented the design, implementation, and characterization stages of a hybrid PIC for a SCORE-SAR receiver. Several system architectures have been considered and simulated, out of which, two were selected because they offer distinct advantages in terms of the system gain and the required LO frequency. By creatively designing the filters, it was possible to translate the two chip architectures into one generic functional design, which was converted into a $Si_3N_4$ (TriPleX) mask design. As part of the risk mitigation plan, two versions of $Si_3N_4$ mask designs were created: a PZT-based one, and a heater-based one. After that, LXI fabricated the $Si_3N_4$ chips, and built several hybrid PIC assemblies out of the $Si_3N_4$ and the InP chips. Further, LXI designed and implemented the PCBs and the driving electronics and the software that controls them.

The Spacebeam assemblies are capable of realizing two main functionalities: reconfigurable beamforming and frequency down-conversion. The focus of this article was on demonstrating the frequency down-conversion functionality, where several building blocks were tuned, such as the laser, the filters, the Blass matrix, and the splitters, then, an RF signal in the X-band was applied to the hybrid assembly, and it was successfully down-converted into an IF at 1.35 GHz.

The measured down-conversion gain was significantly lower than the simulated one, mainly, due to the lower output power

from the laser. The simulations assumed 18 dBm output power from the laser, which was based on measurement data of lasers with heater-based actuators, while the actuators of the assembly presented in this article are PZT-based. Although this is a major breakthrough, since it is the first demonstration of a PZT-based laser, the measured output power of the laser was considerably lower than the heater-based ones. This could be due to the extra losses in the laser cavity; it is being investigated and is expected to improve in the near future.

More modules have been fabricated and assembled including one with heater-based TriPleX, which is expected to have much more laser power ($>$18 dBm), and thus, more system gain, but it will dissipate more power. These modules are currently being characterized with the goal of demonstrating beamforming and higher conversion gain.

The key technical future developments that will be addressed in future studies and collaborations reflect: i) further improvement of the fabrication of even lower-loss silicon nitride PICs, in combination with monolithic efficient low-power PZT-actuators, ii) integration of improved high speed modulators with reduced insertion losses and optimized mode field matching to the TriPleX PIC to reduce interface loss (currently 4 dB), iii) co-design of RF circuitry (PCBs and low noise amplifiers and transimpedance amplifiers) and miniaturization of the RF-photonics module iv) assessment of hermetically sealed packaging solutions to come to a full space-compliant engineering qualified model (EQM) solution.

## References

[1] H.-D. Guo, L. Zhang, and L.-W. Zhu, "Earth observation Big Data for climate change research," *Adv. Climate Change Res.*, vol. 6, no. 2, pp. 108–117, 2015, doi: 10.1016/j.accre.2015.09.007.

[2] K. Anderson, B. Ryan, W. Sonntag, A. Kavvada, and L. Friedl, "Earth observation in service of the 2030 agenda for sustainable development," *Geo-Spatial Inf. Sci.*, vol. 20, no. 2, pp. 77–96, 2017, doi: 10.1080/10095020.2017.1333230.

[3] A. Moreira, P. Prats-Iraola, M. Younis, G. Krieger, I. Hajnsek, and K. P. Papathanassiou, "A tutorial on synthetic aperture radar," *IEEE Geosci. Remote Sens. Mag.*, vol. 1, no. 1, pp. 6–43, Mar. 2013, doi: 10.1109/MGRS.2013.2248301.

[4] S. Kutty and D. Sen, "Beamforming for millimeter wave communications: An inclusive survey," *IEEE Commun. Surv. Tuts.*, vol. 18, no. 2, pp. 949–973, Secondquarter 2016, doi: 10.1109/comst.2015.2504600.

[5] H. Nishimoto et al., "Performance evaluation of NL-BMD precoding over analog-digital hybrid beamforming for high SHF wide-band massive MIMO IN 5G," *Int. J. Wireless Inf. Netw.*, vol. 24, no. 3, pp. 225–239, 2017, doi: 10.1007/s10776-017-0364-1.

[6] P. Ghelfi et al., "A fully photonics-based coherent radar system," *Nature*, vol. 507, no. 7492, pp. 341–345, 2014, doi: 10.1038/nature13078.

[7] A. C. Paolella et al., "Hybrid integration of RF photonic systems," *J. Lightw. Technol.*, vol. 36, no. 21, pp. 5067–5073, Nov. 2018, doi: 10.1109/JLT.2018.2870252.

[8] S. Li et al., "Chip-based microwave-photonic radar for high-resolution imaging," *Laser Photon. Rev.*, vol. 14, no. 10, 2020, Art. no. 1900239, doi: 10.1002/lpor.201900239.

[9] L. Bliek et al., "Automatic delay tuning of a novel ring resonator-based photonic beamformer for a transmit phased array antenna," *J. Lightw. Technol.*, vol. 37, no. 19, pp. 4976–4984, Oct. 2019, doi: 10.1109/jlt.2019.2926621.

[10] S. Huber, "Spaceborne SAR systems with digital beamforming and reflector antenna," *Deutsches Zentrum für Luft- und Raumfahrt*, Feb. 2014. Accessed: Jun. 5, 2023. [Online]. Available: https://elib.dlr.de/93190/

[11] T. Otto et al., "Microwave photonics beamformer for spaceborne SAR," in *Proc. IEEE 14th Eur. Conf. Synthetic Aperture Radar*, 2022, pp. 1–3.

[12] "Space SAR system with reconfigurable integrated photonic beamforming," SPACEBEAM, 2020. Accessed: Jun. 5, 2023. [Online]. Available: https://www.spacebeam-project.eu/

[13] T. Otto et al., "SPACEBEAM optical beamformer for SAR–A potential enabler for the SKADI mission," in *Proc. 7th Workshop RF Microw. Syst., Instrum. Sub-Syst. + 5th Ka-Band Workshop Organized ESA-ESTEC*, May 2022, pp. 1–5.

[14] N. Hosseini et al., "Stress-optic modulator in Triplex platform using a piezoelectric lead zirconate titanate (PZT) thin film," *Opt. Exp.*, vol. 23, no. 11, 2015, Art. no. 14018, doi: 10.1364/oe.23.014018.

[15] M. Reza et al., "Design and performance estimation of a photonic integrated beamforming receiver for scan-on-receive synthetic aperture radar," *J. Lightw. Technol.*, vol. 39, no. 24, pp. 7588–7599, Dec. 2021, doi: 10.1109/jlt.2021.3119225.

[16] J. Blass, "Multidirectional antenna - A new approach to stacked beams," in *Proc. IRE Int. Conv. Rec.*, 1960, pp. 48–50, doi: 10.1109/irecon.1960.1150892.

[17] Y. J. Guo, M. Ansari, and N. J. G. Fonseca, "Circuit type multiple beamforming networks for antenna arrays in 5G and 6G terrestrial and non-terrestrial networks," *IEEE J. Microw.*, vol. 1, no. 3, pp. 704–722, Jul. 2021, doi: 10.1109/jmw.2021.3072873.

[18] M. Reza et al., "Design of an integrated-photonics RF beamformer for multi-beam satellite synthetic aperture radar," in *Proc. IEEE Topical Meeting Microw. Photon.*, 2020, pp. 87–90, doi: 10.23919/MWP48676.2020.9314435.

[19] C. Tsokos et al., "Analysis of a multibeam optical beamforming network based on blass matrix architecture," *J. Lightw. Technol.*, vol. 36, no. 16, pp. 3354–3372, Aug. 2018, doi: 10.1109/jlt.2018.2841861.

[20] S. Mosca, F. Bilotti, A. Toscano, and L. Vegni, "A novel design method for Blass matrix beam-forming networks," *IEEE Trans. Antennas Propag.*, vol. 50, no. 2, pp. 225–232, Feb. 2002.

[21] C. G. H. Roeloffzen et al., "Low-loss $SI_3N_4$ triplex optical waveguides: Technology and applications overview," *IEEE J. Sel. Topics Quantum Electron.*, vol. 24, no. 4, Jul./Aug. 2018, Art. no. 4400321, doi: 10.1109/jstqe.2018.2793945.

[22] V. J. Urick, J. D. Mckkiney, and K. J. Williams, "External intensity modulation with direct detection," in *Fundamentals of Microwave Photonics*, 1st ed. Hoboken, NJ, USA: JWS, 2015, ch. 6, sec. 2, pp. 218–222.

[23] Y. Fan et al., "Hybrid integrated INP-$Si_3N_4$ diode laser with a 40-hz intrinsic linewidth," *Opt. Exp.*, vol. 28, no. 15, pp. 21713–21728, 2020, doi: 10.1364/oe.398906.